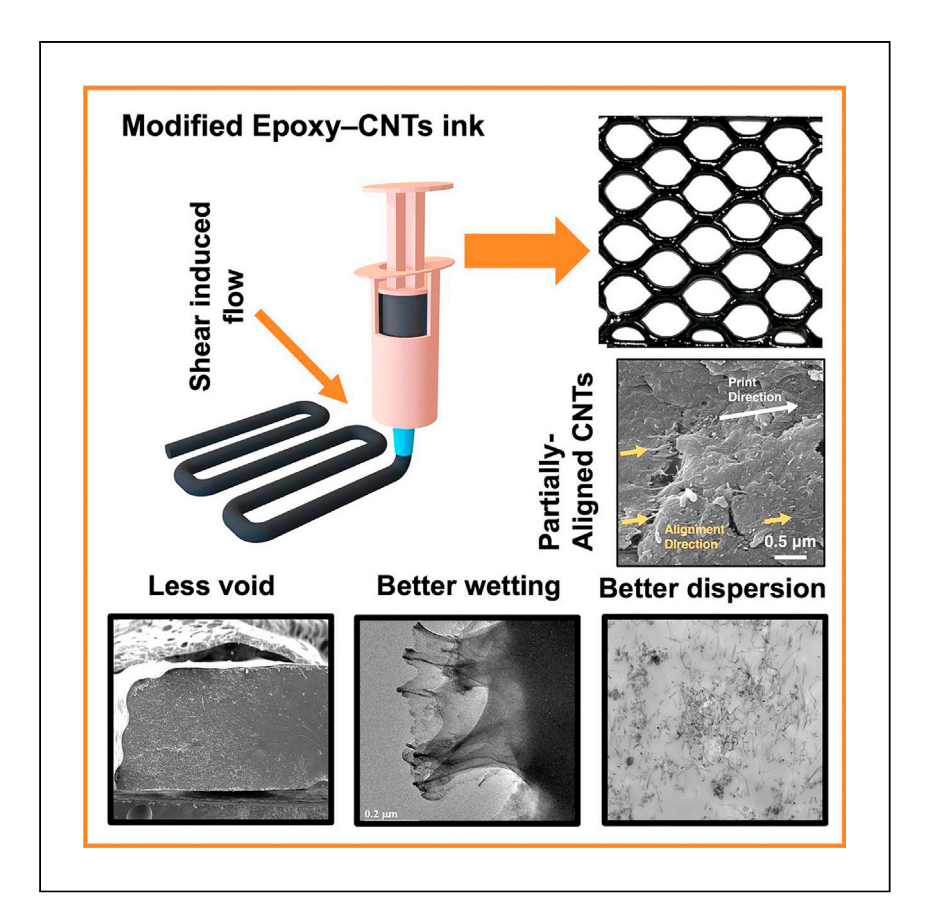


Article

Processing dynamics of carbon nanotubeepoxy nanocomposites during 3D printing



Khater et al. investigate the effect of direct ink writing on the microstructural development of epoxy-CNT nanocomposites with a particular focus on void reduction, better dispersion, wetting, and partial alignment of the CNTs, which results in enhanced mechanical and thermal properties of the nanocomposites compared to their mold-cast counterparts.

Ali Zein Khater, M.A.S.R. Saadi, Sohini Bhattacharyya, ..., Hanyu Zhu, Pulickel M. Ajayan, Muhammad M. Rahman

ajayan@rice.edu (P.M.A.) maksud@rice.edu (M.M.R.)

Highlights

CNT-epoxy nanocomposite structures are developed via direct ink writing (DIW)

High shear stress on ink through nozzle facilitates void reduction in nanocomposite

DIW facilitates better dispersion, wetting, and partial alignment of CNTs

Microstructural changes improve mechanical and thermal properties of nanocomposite

Khater et al., Cell Reports Physical Science 4, 101617

October 18, 2023 © 2023 The Author(s). https://doi.org/10.1016/j.xcrp.2023.101617





Article

Processing dynamics of carbon nanotube-epoxy nanocomposites during 3D printing

Ali Zein Khater, ¹ M.A.S.R. Saadi, ¹ Sohini Bhattacharyya, ¹ Alex Kutana, ¹ Manoj Tripathi, ² Mithil Kamble, ³ Shaowei Song, ⁴ Minghe Lou, ⁵ Morgan Barnes, ¹ Matthew D. Meyer, ⁶ Vijay Vedhan Jayanthi Harikrishnan, ¹ Alan B. Dalton, ² Nikhil Koratkar, ³ Chandra Sekhar Tiwary, ⁷ Peter J. Boul, ⁸ Boris Yakobson, ¹ Hanyu Zhu, ¹ Pulickel M. Ajayan, ^{1,*} and Muhammad M. Rahman^{1,9,*}

SUMMARY

Carbon nanotube (CNT)-reinforced polymer nanocomposites are promising candidates for a myriad of applications. Ad hoc CNT-polymer nanocomposite fabrication techniques inherently pose roadblocks to optimized processing, resulting in microstructural defects, i.e., void formation, poor interfacial adhesion, wettability, and agglomeration of CNTs inside the polymer matrix. Here, we show that a 3D printing technique offers improved processing of CNTpolymer nanocomposites. During printing, the shear-induced flow of an engineered nanocomposite ink through the micronozzle is beneficial, as it reduces the number of voids within the epoxy matrix, improves CNT dispersion and adhesion with epoxy, and partially aligns the CNTs. Such microstructural changes result in enhanced mechanical and thermal properties of the nanocomposites compared to their mold-cast counterparts. This work demonstrates the advantages of 3D printing in achieving improved processing dynamics for the fabrication of CNT-polymer nanocomposites with better structural and functional properties.

INTRODUCTION

Carbon nanotubes (CNTs) demonstrate remarkable mechanical, thermal, electronic, and optical properties, resulting in their widespread application across many disciplines.¹⁻⁴ Particularly, CNTs are promising fillers as mechanical reinforcement in polymer composites because of their high modulus, strength, specific surface area, and aspect ratio. 1,2 However, CNT-reinforced composites for structural applications have been limited due to poor matrix-reinforcement interfacial adhesion, wettability, and agglomeration of the CNTs within the matrix material.³⁻⁶ These challenges are difficult to overcome since the very same properties that make CNTs promising lead to these inherent flaws. For instance, the high specific surface area of CNTs provides a desirable interface for stress transfer in polymer composites. However, it also leads to strong attractive forces among CNTs, which entangle CNTs and produce a bundling effect called agglomeration. ^{7,8} This makes it difficult to achieve uniform dispersion of CNTs in the polymer phase, limiting the efficiency of CNTs in the polymer matrices and ultimately weakening the composites. Various mechanical methods such as ultra-sonication, ball-milling, and high shear mixing have been adopted to disperse CNTs in polymers. 9-11 Besides, chemical functionalization of CNTs' surface improved CNT-matrix interfacial interaction and dispersion

https://doi.org/10.1016/j.xcrp.2023.101617



¹Department of Materials Science and NanoEngineering, Rice University, Houston, TX 77030, USA

²Department of Physics and Astronomy, University of Sussex, Brighton BN1 9RH, UK

³Department of Mechanical, Aerospace and Nuclear Engineering, Rensselaer Polytechnic Institute, Troy, NY 12180, USA

⁴Department of Physics, University of Houston, Houston, TX 77204, USA

⁵Department of Electrical and Computer Engineering, Rice University, Houston, TX 77030,

⁶Shared Equipment Authority (SEA), Rice University, Houston, TX 77030, USA

⁷Metallurgical and Materials Engineering, Indian Institute of Technology Kharagpur, West Bengal 721302, India

⁸Aramco Americas, Houston, TX 77002, USA

⁹Lead contact

^{*}Correspondence: ajayan@rice.edu (P.M.A.), maksud@rice.edu (M.M.R.)





of CNTs in the matrix. 12-14 However, these processes have limitations and can pose several challenges, i.e., void formation, high viscosity, limited processability, and, consequently, compromised mechanical and thermal properties.

3D printing is a rapidly growing manufacturing technology due to its versatility and ability to produce complex structures with controlled microstructures and properties. 15-17 It is also known as a sustainable manufacturing process, as it reduces material waste and eliminates structural support for complex shaping, e.g., a physical mold. Among the different 3D-printing methods, extrusion-based printing techniques such as fused filament fabrication (FFF) and direct ink writing (DIW) enable the fabrication of 3D structures with intricate cellular architectures. In both processes, the material is selectively dispensed through a nozzle or orifice in a layerby-layer fashion at the macro-, meso-, and microscales. FFF is a heat-assisted extrusion-based technique that works by melting a continuous filament and depositing it on a substrate. FFF-printed structures often suffer from defects such as shrinkage and warping. Unlike FFF, DIW does not require a heat source and has emerged as a more versatile printing technique that can develop 3D structures from a wide variety of materials. ^{18–21} One of the main challenges of DIW is to design and formulate viscoelastic inks that can easily flow through a nozzle under shear and quickly recover upon deposition. Therefore, the ink needs to demonstrate a non-Newtonian, shearthinning behavior for extrusion while possessing a sufficiently high storage modulus to maintain the printed filamentary shape after extrusion.²² The ink also needs to exhibit yield flow behavior such that the ink requires a certain amount of stress to be applied before it begins to flow. With an optimized ink, DIW allows superior control over the composition, shape, and geometry of polymer composites, giving it an edge over traditional fabrication methods. Additionally, this extrusion-based technique is favored because shear-induced alignment during printing can be leveraged to align fillers during extrusion, resulting in high-performance anisotropic composites.^{23–26} Since shear-induced flow is intrinsically coupled to the DIW process, it is imperative to understand the effect of shear stresses on void formation, adhesion, dispersion, and alignment of anisotropic reinforcements in the polymer phase during printing of composite structure. Understanding the dynamics of the printing process and its effect on composite processing is critically important for 3D printing of composites with better physical properties.

Extrusion-based additive manufacturing (AM) methods have been used to 3D print CNT-polymer composites. Recently, for instance, CNT-epoxy composites were 3D printed using a modified FFF technique. This method melted the solid epoxy resin to extrude; however, the final 3D printed structures suffered from significant void formation.²⁷ In another work, CNT-epoxy composites were printed using DIW. However, the primary objective of this study was showcasing how CNTs can be used as a radio frequency (RF)-absorbing unit within an uncured polymer system to establish RF heating as an alternative to conventional curing.²⁸ Furthermore, this work did not discuss the effect of the printing process on the final microstructure and properties of the nanocomposites.

Here, we design a rheologically modified CNT-epoxy nanocomposite ink to 3D print architected structures via DIW and compare the properties of printed composites with the conventional mold-cast counterparts. The processing dynamics during printing and the effect of printing on the microstructures of the composites have been investigated thoroughly. The tapered nozzle imparts high shear stress on the ink during the printing process, which reduces voids in the structure significantly. Furthermore, 3D printing facilitates better dispersion, wetting, and partial alignment

Article



of the CNT fillers in the composite structure, which ultimately provides greater mechanical strength to the structure. Using optical and electron microscopy techniques coupled with Raman spectroscopy, UV-visible (UV-vis) spectroscopy, and theoretical simulations, we provide direct evidence of the improved processing dynamics, i.e., void reduction, better dispersion, improved CNT-epoxy wetting, and partial alignment of CNTs during DIW of modified CNT-epoxy nanocomposites. Consequently, the 3D-printed structures demonstrate superior mechanical and thermal performance as compared to their mold-cast counterparts due to improved microstructures.

RESULTS AND DISCUSSION

DIW of CNT-epoxy nanocomposites

In this work, an epoxy resin was used as the matrix phase because epoxies are widely regarded for their high stiffness, strength, chemical resistance, low cost, and versatile polymerization routes.^{29,30} Our investigation commenced through the evaluation of the printability of the inks containing varying concentrations (0, 0.1, 0.3, and 1 wt %) of CNTs (Figure 1A). The pristine epoxy behaves as a Newtonian fluid and lacks the necessary rheological properties required for DIW (Figure 1B). After dispersing CNTs in the epoxy matrix, the ink demonstrated an increase in viscosity and showed slight shear-thinning behavior (ink formulation can be found in the experimental procedures section). However, the CNT-epoxy ink cannot be printed successfully at this stage (Figure 1C) since the ink is not able to retain the filamentary shape after extrusion due to low storage (G') and loss modulus (G"). Typically, DIW requires that the ink demonstrates shear-thinning behavior, an optimum viscosity, and suitable storage and loss modulus to allow for extrusion at low pressures while maintaining its shape after printing.²¹ Ideally, the ink should possess sufficiently high G' and G'', and there should be a cross-over point between the G' and G'' as a function of shear rate. During extrusion, when the force is applied (high shear rates), the loss modulus is higher, and the ink acts more fluid-like. On the other hand, after printing, when the applied force is removed (low/no shear rates), the storage modulus is higher, and the ink acts as a solid, retaining the extruded filamentary shape.³¹ To attain printability, the inks were modified by adding a rheology modifier.³² Typically, rheology modifiers modify the microstructure of composites through the formation of weak physical bonds. At optimized loading of rheology modifiers, a material can be formed as a viscoelastic solid that behaves like a solid but transitions into a liquid-like material under applied stress, when physical bonds between modifier clusters break. 33-36 A commonly used rheology modifier for DIW of epoxy and other polymers²³ is fumed silica, which forms interlocking clusters^{37–39} and can be used to suspend other second-phase reinforcement particles within the matrix.⁴⁰ This is advantageous in our case as it can retain the position of CNTs after extrusion. We fabricated epoxy nanocomposites loaded with the same weight fraction of fumed silica in both mold-cast and 3D-printed specimens. Note that the addition of fumed silica is known to deteriorate mechanical and thermal properties of base polymers.³⁷ Therefore, the ink formulation was optimized to have the minimum amount of silica (8.5 wt %) that renders printability to the ink.

Rheology analysis of the modified ink revealed the highly shear-thinning (Figure 1B) and shear-yielding (Figure 1C) behavior of the ink that is ideal for smooth flow during printing without clogging the micronozzle. The relationship between the apparent viscosity and the shear rate as shown in Figure 1B follows the power-law model²¹ $\eta = K \dot{\gamma}^{n-1}$, where, η is the viscosity, K is the flow consistency index, $\dot{\gamma}$ is the shear rate, and n is the power-law index. Typically, for shear-thinning fluids, n fits the



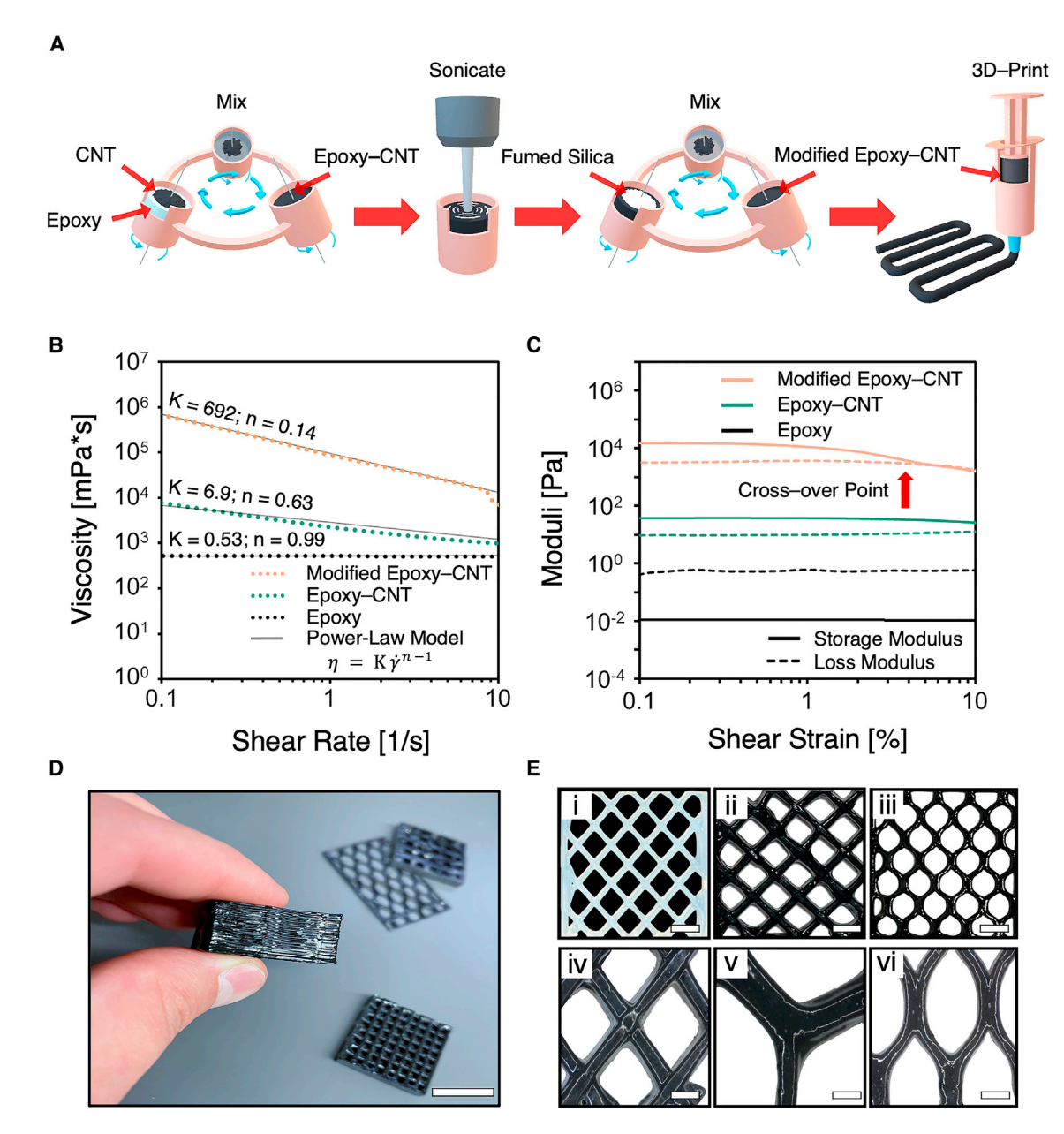


Figure 1. DIW of modified CNT-epoxy nanocomposites

- (A) Schematic diagram depicting the various steps of modified CNT-epoxy nanocomposite fabrication via DIW.
- (B) Apparent viscosity as a function of shear rate for modified epoxy-CNT, epoxy-CNT, and epoxy inks, which follows the power-law model.
- (C) Storage (solid line) and loss (dotted line) modulus of modified epoxy-CNT, epoxy-CNT, and epoxy ink as a function of oscillation strain.
- (D) Photograph of various 3D-printed modified CNT-epoxy nanocomposite structures showing the layer-by-layer assembly. Scale bar: 1 cm.
- (E) Photographs and optical microscopy images of 3D-printed architected structures: (i) rectilinear structure of epoxy polymer (modified), (ii) rectilinear and (iii) hexagonal honeycomb structures of modified CNT-epoxy nanocomposites, and (iv–vi) zoomed-in optical microscopy images of nodes of 3D-printed modified CNT-epoxy nanocomposites. Scale bars: (i–iii) 4 mm and (iv–vi) 2 mm.

parameter 0 < n < 1, while for Newtonian fluids, n = 1. The viscoelastic behavior (Figure 1C) of the modified ink also improved, meaning that G' at low strain for the modified CNT-epoxy ink is one order of magnitude greater than G'', which is required for retaining the shape after extrusion. Moreover, the cross-over point for the modified CNT-epoxy nanocomposite ink occurs at a low enough shear strain (7%) and/or

Article



shear stress (2.4 × 10³ Pa) as to enable printing using typical low extrusion forces (Figure 1C). After the rheology of the ink was optimized, modified CNT-epoxy nanocomposites with architectures such as rectilinear and honeycomb structures were 3D printed (Figures 1D, 1Eii, and 1Eiii; see Video S1 for a video of the 3D-printing process). Figure 1Ei shows that architected structures can also be developed from epoxy resin once the rheology has been modified (see Video S2 for a video of the 3D-printing process). The zoomed-in optical images of the nanocomposite structures, as shown in Figures 1Eiv–1Evi, demonstrate that the modified ink can be used for high-resolution printing of 3D structures with smooth and continuous edges of extruded filaments. Following the extrusion, the structures were thermally cured to ensure better bonding between the printed layers and overall hardening of the 3D objects (see experimental procedures section for curing protocol).

Morphology and microstructure of 3D-printed CNT-epoxy nanocomposites

Next, we evaluated the morphology and microstructure of the mold-cast and 3Dprinted modified CNT-epoxy nanocomposites using a holistic approach that combined optical microscopy, X-ray computed tomography (CT scan), transmission electron microscopy (TEM), Raman spectroscopy, UV-vis spectroscopy, and scanning electron microscopy (SEM). Typically, epoxies with increasing concentrations of nanofiller materials, such as CNTs, are susceptible to void formation during processing.² Strong particle-particle interaction leads to an increase in viscosity in the polymer nanocomposites with increasing CNT concentrations, which hinders the removal of entrapped bubbles from the composite. This leads to the formation of voids in the final composites, which act as stress concentration zones and can lead to catastrophic failure. Use of heat, mechanical vibration, sonication, or vacuum to remove voids has proven to be ineffective, leaving behind residual voids in the composite structure.⁶ Thus, removal of voids remains a challenge in conventional manufacturing processing for fabrication of CNT-polymer composites with a high viscosity. We therefore investigated void formation in composites fabricated via a conventional technique (mold casting) and via 3D printing (DIW) with identical composition. SEM micrographs of the fracture surface revealed significant void formation in the mold-cast samples (Figure 2A), while the printed nanocomposites showed reduced void formation (Figure 2B). Similar observations were made from the CT scan images of mold-cast and 3D-printed nanocomposites (Figure S1). The high shear force exerted during the DIW process is responsible for the reduction of voids in the printed structure. As the ink passes through the micronozzle, the voids and air pockets experience structural distortion under the fluidic shear stress. This is followed by collapsing due to the in-plane confinement along the tapered channel (see Video S3 and Figure S2 for observing the collapse of voids during 3D printing). This leads to significant reduction of the voids in the 3D-printed structures. The effect of 3D printing on the reduction of microstructural voids can be better observed when the mold-cast and 3D-printed samples without CNTs are analyzed and compared (Figure 1Ei; Video S2). The optical microscopy images show that the mold-cast epoxy sample has high void concentrations, while the 3D-printed sample does not possess the same degree of void formation (Figure S3). Furthermore, the absence of inter-filament voids in the fracture surface of the printed samples indicates full coalescence of the filaments under shear during deposition (Figure 2B). These findings clearly show that DIW has an inherent benefit of reducing void formation compared to conventional mold-casting techniques.

In order to employ CNTs as effective reinforcements in polymer composites, CNT-polymer interfacial adhesion and proper dispersion of CNTs in the polymer matrix are among the most critical factors.^{5,11} Poor interfacial adhesion results in



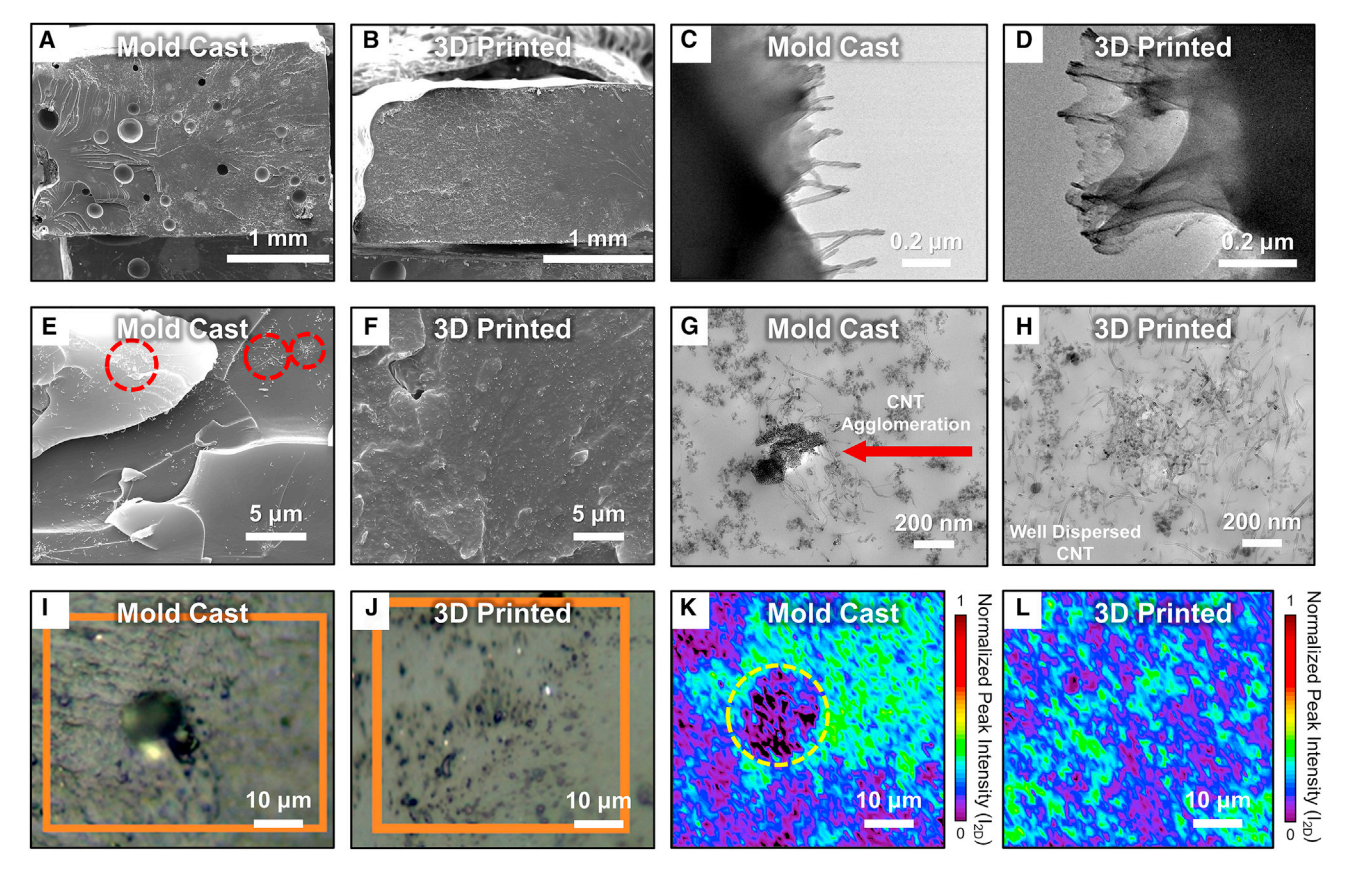


Figure 2. Morphology and microstructure of mold-cast and 3D-printed modified CNT-epoxy nanocomposites

(A and B) Scanning electron microscopy (SEM) images of cross-section of mold-cast and 3D-printed samples showing void reduction in 3D-printed sample.

(C and D) Transmission electron microscopy (TEM) images of CNT pullout in mold-cast and 3D-printed samples.

(E and F) SEM images of the fractured surfaces of mold-cast and 3D-printed samples showing poor dispersion in the mold-cast sample compared with in the 3D-printed sample. Poorly dispersed CNTs are marked by dashed circles (red) in (E).

(G and H) TEM micrographs of (G) mold-cast and (H) 3D-printed samples. The mold-cast sample shows agglomeration (marked by arrow) of CNTs. Also, most of the regions of the mold-cast sample show the absence of CNTs, indicating poor dispersion. In the 3D-printed sample, there is better dispersion of CNTs without any cluster formation.

(I and J) Optical image of mold-cast and 3D-printed samples. The orange square marks the area where Raman spectroscopic measurements were carried out.

(K and L) Raman mapping (I_{2D}) of mold-cast and 3D-printed modified CNT-epoxy nanocomposites. The dashed circle (yellow) in (K) represents a void in the Raman image. Normalized 2D peak intensity (I_{2D}) reveals the distribution of CNTs, where $I_{2D} = 0$ shows the absence of CNTs.

inadequate load transfer between polymer and CNTs, while poorly dispersed CNTs can agglomerate, thereby having a direct impact on the physical properties and the performance of the composites. In our work, a high-resolution TEM was used to analyze both mold-cast and 3D-printed samples to gain insight about the CNT-polymer interfacial adhesion. As shown in Figure 2C, the mold-cast sample revealed CNT pullout, suggesting poor wetting or adhesion between the polymer matrix and the CNTs. Conversely, for the 3D-printed sample, CNT pullouts were wetted (enclosed) by the epoxy resin, indicating better adhesion of the CNTs with the matrix (Figure 2D). This is a direct consequence of the constrictive pressure during extrusion that ensures a forced interaction between the CNTs and the polymer matrix. Under the presence of high shear forces, the interfacial interaction between CNTs and polymer has been improved. As such, during CNT pullout, the polymer matrix was pulled with the CNTs. This phenomenon is not observed in the mold-cast sample.

Article



Improving the CNT-epoxy interfacial interaction is expected to improve the mechanical and thermal properties of the nanocomposites, ^{42,43} as we will observe further on.

In order to determine the degree of CNT dispersion in the epoxy matrix for moldcast and 3D-printed samples, we investigated the distribution of CNTs in the polymer matrix by observing the fracture surface under SEM, TEM, and Raman spectroscopy. The morphologies of the fracture surface of mold-cast and 3D-printed samples under an SEM are presented in Figures 2E and 2F, respectively. From Figure 2E, clusters of CNTs are seen in the mold-cast sample (marked with red dashed circles), and little or no CNTs are visible in the relatively smooth region of the fracture surface. This illustrates uneven distribution of CNTs in the mold-cast samples, suggesting poor dispersion and agglomeration. In contrast, the 3D-printed sample showed the presence of well-dispersed CNTs throughout the epoxy resin (Figure 2F). To further investigate the dispersion of CNTs, TEM micrographs of both mold-cast and 3D-printed samples were analyzed. A TEM image of the mold-cast sample clearly shows CNT agglomeration (Figures 2G and 2H). There is significant entanglement between CNTs, forming CNT clusters, while most other areas do not have any CNTs. This suggests poor dispersion in the mold-cast specimen. On the other hand, the 3D-printed sample highlights well-dispersed CNTs. The better dispersion is made more evident by observing the surrounding. Contrary to the mold-cast sample, the surrounding area in the 3D-printed sample contains a fair dispersion of CNTs and does not form a dense CNT cluster. Therefore, it can be said that DIW improves the dispersion of CNTs within the polymer matrix.

The differences observed under SEM and TEM are further corroborated by Raman spectroscopy. The penetration depth of the Raman laser used for the measurement was up to 100 µm, which allowed the detection of embedded CNTs in either sample. 44,45 Both samples exhibit typical peaks for CNTs, with a G-peak at \sim 1,590 cm $^{-1}$ and a D-peak at \sim 1,350 cm $^{-1}$, in addition to peaks for epoxy and fumed silica (Figure S4A). 46 However, the 2D peak (~2,688 cm⁻¹) for CNTs, which was pronounced for CNT-epoxy nanocomposites, was not observed for epoxy samples. Therefore, the 2D peak intensity (I_{2D}) was used to indicate the spatial distribution of CNTs in different samples. 47 The optical images of the mold-cast and 3Dprinted samples are shown in Figures 2I and 2J, respectively, and the orange square in these images depicts the region where the Raman spectroscopic mapping was conducted. The I_{2D} distribution map shows agglomeration, or poor dispersion, of CNTs in the mold-cast samples, which is evident in Figure 2K, through the confined area of bright cyan regions in the vicinity of the voids (marked with a yellow dashed circle). Moreover, since the number of voids is higher, the agglomeration, or poor dispersion, of CNTs in the mold-cast sample is also significant, especially around the voids. On the contrary, the 3D-printed specimen reveals a uniform dispersion (Figure 2L) of CNTs across the mapped surface (more uniformly distributed bright cyan regions). Furthermore, the comparison of individual Raman spectra of CNT powders and mold-cast and printed samples (Figure S4A) exhibits a gradual upshift in the G-peak positions from powdered CNTs $(1,586.6 \text{ cm}^{-1})$ to the printed sample (1,607.6 cm⁻¹), with an intermediate value for mold-cast samples (1,594.6 cm⁻¹). The observed shift in the frequency (cm⁻¹) of Raman modes of CNTs could be interpreted to estimate the interaction between CNTs: shifting toward a higher frequency corresponds to a lesser CNT-CNT interaction, which reflects the state of dispersion or disentanglement. 48 Since the highest shifting was observed for the 3D-printed samples, it can inferred that CNTs are relatively more disentangled in the printed sample compared with the CNT powders and the mold-cast sample. We have also



observed a similar trend in peak frequency shifting (Figures S4D and S4E) for a large scan area of the sample. In the mold-cast sample, an ~36% region of areal mapping illustrates the upshifting of the prominent G Raman mode of CNTs, while for the printed samples, an ~72% region in the mapped area shows the upshift (Raman spectroscopic image analysis details can be found the experimental procedures section). Thus, the epoxy matrix of the printed sample leads to a greater disentanglement in nanotubes, suggesting better dispersion in the printed sample as compared with the mold-cast sample. During extrusion, the induction of high shear forces deagglomerates CNTs, ¹¹ while the presence of yield stress in the ink helps to prevent the CNTs from re-agglomeration. The magnitude of the forces at the yield point in the ink is expected to exceed the relatively weak van der Waals forces of CNTs responsible for their agglomerations, thereby improving the overall dispersion of the CNTs.

In order to provide a quantitative analysis of the dispersion of the CNTs in the mold-cast and 3D-printed samples, UV-vis spectroscopy ⁴⁹ was also employed. From the UV-vis spectra (Figure S5), we observe that the 3D-printed ink has higher absorbance throughout the entire range of the wavelength of light used in the study. Consequently, the area below the UV-vis spectrum line was also greater for the 3D-printed ink. This suggests that the extruded 3D-printed ink has more dispersed CNTs compared with the mold-cast samples. ^{49,50} Furthermore, using the Beer-Lambert law, the degree of the dispersion of CNTs can be analyzed quantitively. In our case, for mold-cast samples, the degree of dispersion was found to be 25.5%–28.5%, while that for the 3D-printed sample was 52.73%–58.96% (details can be found in the experimental procedures section and in the supplemental information). This shows a nearly 2-fold improvement in the dispersion of CNTs for the 3D-printed sample compared with the mold-cast sample.

Previous studies on DIW of nanocomposites have shown that the shear forces arising during extrusion through the micronozzle align nanofillers, i.e., 2D materials, ⁵¹ MXenes, ²⁶ and cellulose nanocrystals, ²⁴ in the matrix during printing. The alignments in printed structures outperformed composites filled equivalently with randomly oriented fillers. While controlled CNT alignment is difficult to achieve in polymer composites fabricated via conventional techniques, we speculated that it is possible to attain some degree of CNT alignment along the print direction during DIW.²¹ To investigate possible CNT alignments during DIW, a simulation of the extrusion process inside the print nozzle is carried out using the exact experimental parameters. The motion of the epoxy is assumed to be a steady laminar flow, and CNTs are represented as prolate rigid particles with an aspect ratio *l*. The motion of a prolate particle in the shear flow is described by Jeffery's equations and is periodic, with solutions called Jeffery orbits. In cylindrical shear (Poiseuille) flow, the radial velocity distribution u(r) is given by

$$u(r) = 2\langle u \rangle (1 - r^2 / r_0^2).$$
 (Equation 1)

Here, r_0 is the radius of the cylinder, and $\langle u \rangle$ is the average velocity of the flow.

Due to forces from the liquid acting on the particle, its ends engage in a paddle-like periodic motion, tracing Jeffery orbits. ⁵² With an increasing aspect ratio of the particle, the orbits become sharper, and the particle spends more time in the alignment along the direction of the flow. The alignment effects are thus strong for CNTs with their extreme aspect ratios. Examples of trajectories (Jeffery orbits) traced by the ends of a rigid particle with aspect ratio I = 158 are shown in Figure 3A. Different



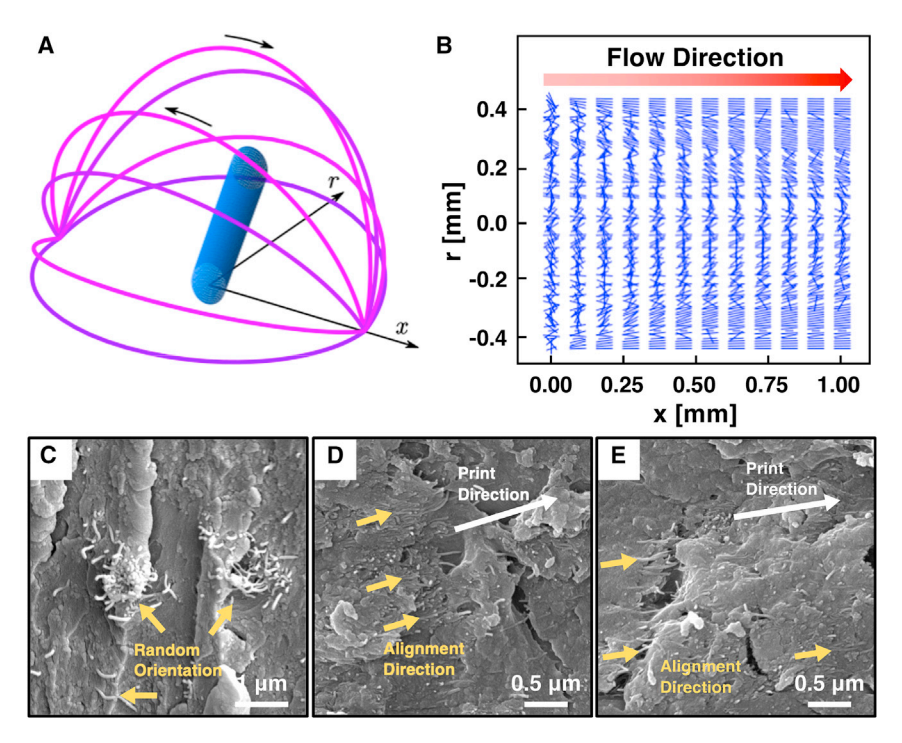


Figure 3. Partial alignment of CNTs in 3D-printed modified CNT-epoxy nanocomposites (A) Jeffery orbits for a rigid particle representing CNT with aspect ratio I = 158 in a shear flow. Different orbits correspond to different initial orientations of the particle. (B) Alignment of CNTs with aspect ratio I = 158 in a Poiseuille flow with radius $r_0 = 0.45$ mm and average velocity < u > = 100 mm/s. Maximum alignment is near the wall, where flow velocity is small. (C–E) SEM images of modified CNT-epoxy nanocomposites in (C) mold-cast samples showing random orientation of CNTs and in (D and E) 3D-printed structures showing partial CNT alignment.

orbits correspond to different initial orientations of the particle. The motion slows down near the turning points where the tube is parallel to the x axis, producing the alignment effect. This alignment effect is illustrated in Figure 3B, showing the solution of Jeffery's equations for CNTs with an aspect ratio I = 158 in a Poiseuille flow having an average velocity $\langle u \rangle = 100$ mm/s in a cylinder with a radius $r_0 = 0.45$ mm. The figure shows the evolution of CNTs starting with random initial orientations and moving along the flow (from left to right) at different radial distances r from the center of the cylinder. The alignment effect is highest near the wall, where shear is maximum. Note that the time spent in alignment with the flow depends on the CNT's aspect ratio and initial orientation but not the shear rate of the flow. To obtain further experimental evidence, SEM images of the surface of dissected mold-cast and 3D-printed samples were analyzed and compared (see the experimental procedures section for sample preparation). While the mold-cast samples showed random orientation of CNTs (Figure 3C), the SEM micrographs provide evidence of partial alignment of CNTs in the 3D-printed sample along the direction of printing (Figures 3D and 3E, shown by marked arrows). This alignment is expected, as shear forces and the extensional flow field that develops within the micronozzle during DIW are known to align anisotropic fillers in a matrix. 41 On the other hand, the mold-cast sample has no external force to induce CNT alignment within the matrix, and hence, the CNTs in the mold-cast specimen are randomly oriented. Note that the poor dispersion and/or agglomeration effects of CNTs are repeatedly observed in the mold-cast sample, consistent with our previous observations (Figure 3C). We anticipate that the improved processing dynamics associated with DIW, i.e., void



reduction, improved interfacial adhesion, CNT dispersion, and partial alignment of CNTs, would enhance the thermal and mechanical properties of the 3D-printed nanocomposites compared with their mold-cast counterparts.

Thermal and mechanical properties of 3D-printed CNT-epoxy nanocomposites

Next, we investigated the thermal properties of mold-cast and 3D-printed modified CNT-epoxy nanocomposites to understand the effect of the above-mentioned morphological and microstructural variations. CNTs are known for their exceptional thermal properties; however, it is known that voids, poor dispersion, agglomeration, and isotropic ordering in composite materials throttle the full potential of CNT-reinforced composites.⁵³ Using the laser flash method,⁵⁴ we obtained the thermal diffusivity and conductivity of the mold-cast and 3D-printed specimens. The thermal conductivity (κ) can be calculated using the relation $\kappa = \rho DC_p$, where ρ is the measured density, C_p is the specific heat capacity, and D is the measured diffusivity (see the experimental procedures section for measurement of density and specific heat capacity). To investigate the effect of shear-induced partial CNT alignment, the test was conducted in two ways: a laser oriented orthogonal (parallel) to the print direction and transverse (perpendicular) to the print direction (Figure 4A). While all three specimens possessed identical composition, mold-cast samples displayed the lowest thermal diffusivity (Figure 4B) and conductivity (Figure 4C). On the other hand, the 3D-printed samples, tested in both ways, showed better thermal properties (Figures 4B and 4C) than the mold-cast samples. Reduced void formation, improved CNT-polymer adhesion, and better CNT dispersion are expected to be responsible for the superior thermal conductivity of the 3D-printed samples. Note that the printed samples with print direction parallel to the laser displayed the highest thermal conductivity. This indicates that the thermal conductivity might be associated with the observed partial CNT alignment along the print direction.

To investigate the heat transfer and dissipation behavior within the structure, in situ surface temperatures of both mold-cast and 3D-printed samples were recorded with a thermal infrared (IR) camera while a white supercontinuum laser (45 mW) was held incident on the samples for light-induced heating. As observed from the thermal mapping images, shown in the inset of Figure 4D, the induced heat is concentrated in a smaller region for mold-cast samples compared with the 3D-printed sample, indicating better heat flow and dissipation within the 3D-printed structure. For comparison, the single-line temperature profiles along the direction marked with blue and red arrows (Figure 4D, inset) for both sample surfaces were extracted from the temperature mapping captured by the IR camera and analyzed for comparison (Figure 4D). When illuminated with a laser of the same power, the line profile of the mold-cast structure showed a higher peak temperature but a smaller full width at half maximum (FWHM) than that of the 3D-printed structure. To observe the time-dependent heat dissipation behavior, temporal changes in the maximum surface temperature were also recorded (Figure 4E), which shows better performance for the 3D-printed nanocomposites. These results clearly show that the 3D-printed samples have superior thermal conductivity and heat dissipation behavior compared with the mold-cast samples.

Finally, the mechanical performances of the mold-cast and 3D-printed nanocomposites containing varying concentrations of CNTs were analyzed and compared. To investigate the potential effects of shear-induced CNT alignment, the tensile bars were 3D printed with different printing paths—one oriented longitudinally along the tensile direction and the other oriented transverse to the tensile direction (Figure S6). The results from the mechanical tests are summarized in Figure 5 (see



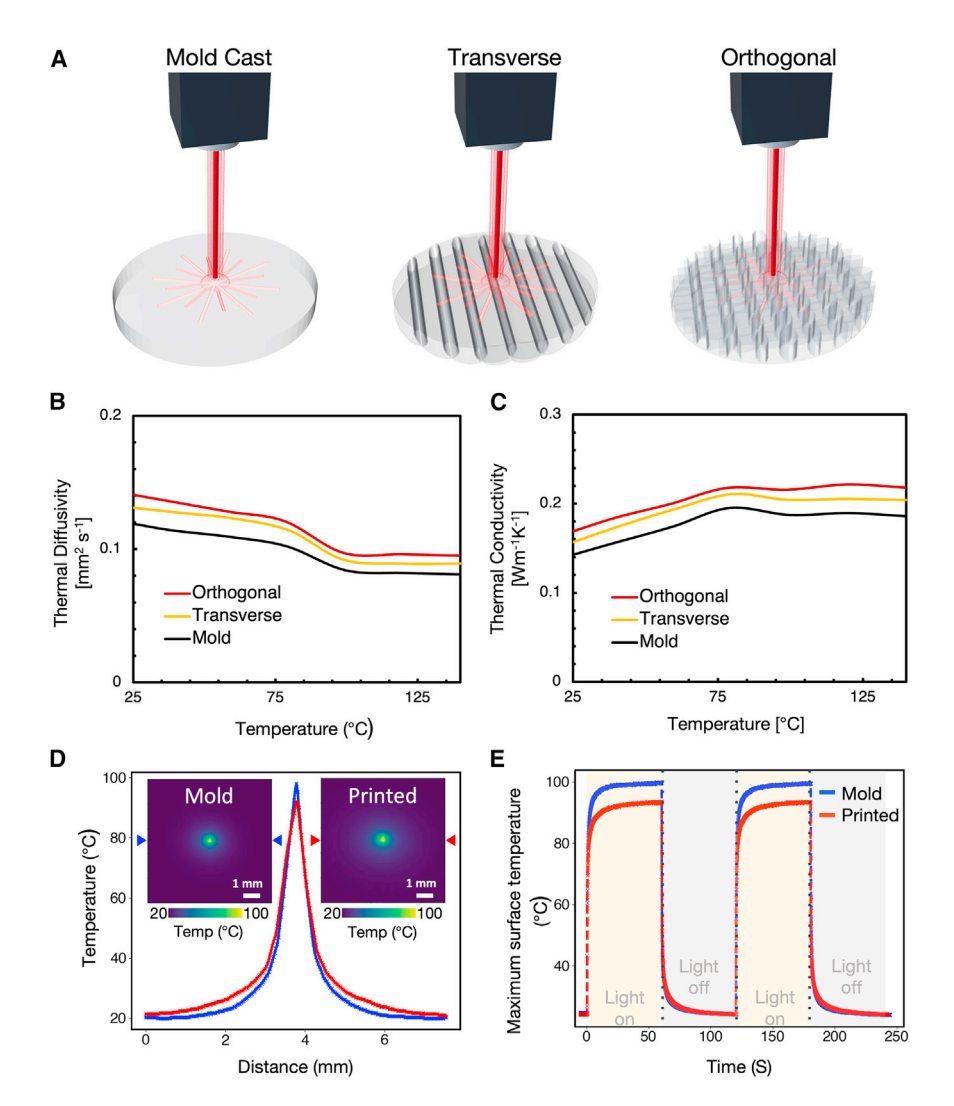


Figure 4. Thermal properties of mold-cast and 3D-printed modified CNT-epoxy nanocomposites (A) Schematic illustration in the laser flash experiments, which depict laser orientation for mold-cast and 3D-printed samples. For 3D-printed samples, the laser is oriented along both transverse (perpendicular) and orthogonal (parallel) directions to the print direction.

- (B) Thermal diffusivity, obtained from the laser flash experiment.
- (C) Thermal conductivity, calculated from thermal diffusivity of mold-cast and 3D-printed samples. (D) Comparison of surface temperature line profile obtained from the thermal infrared (IR) mapping (inset) along the direction marked with blue and red arrows for mold-cast and 3D-printed samples, respectively, under 45 mW laser illumination.
- (E) Comparison of temporal heat dissipation behavior of mold-cast and 3D-printed samples.

Tables S1 and S2 for tabulated values). As illustrated in Figure 5A, the tensile strength for both the mold-cast and 3D-printed samples improved with increasing CNT concentrations. Note that for all wt % of CNT loading, the tensile strength of the 3D-printed samples with either print path is higher than their mold-cast counterparts. The observed difference is attributed to the improved processing dynamics of the DIW technique for the fabrication of CNT-epoxy nanocomposites (Figure 2). The percentage increase in the average tensile strength for the 3D-printed samples evidently shows that the enhancement of the tensile strength is most pronounced for the samples 3D printed with the longitudinal print direction (Table S3). Improvement in the tensile strength is also observed along the transverse direction; however,



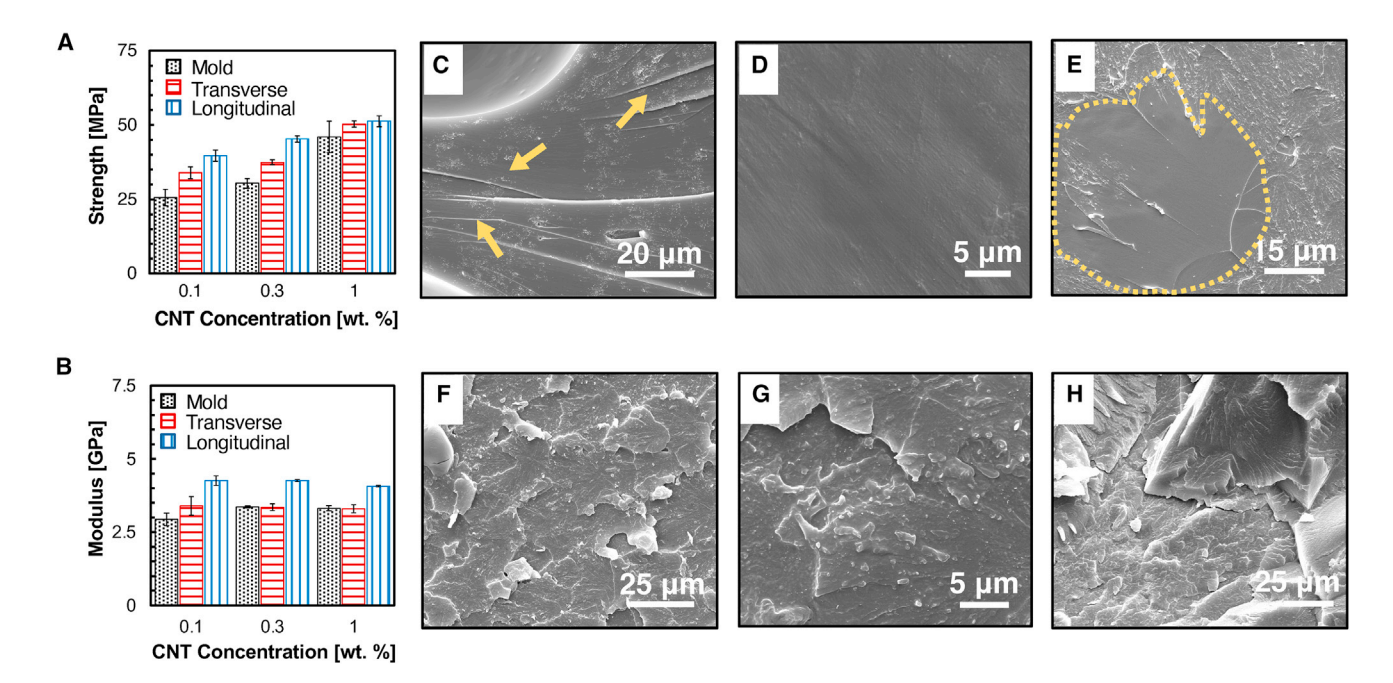


Figure 5. Mechanical properties of mold-cast and 3D-printed modified CNT-epoxy nanocomposites

(A and B) Comparison of (A) tensile strength and (B) Young's modulus of mold-cast and 3D-printed samples (printed along transverse and longitudinal directions) corresponding to different CNT concentrations. The error bars represent the standard error of the samples.

(C-H) Fracture surface analysis of mold-cast (C-E) and 3D-printed samples (F-H) under an SEM. The river-like fracture patterns in mold-cast samples are indicated with yellow arrows in (C). Epoxy-like pockets (without CNTs) observed in mold-cast samples are marked with yellow dashed lines in (E).

the effect is not as pronounced as along the longitudinal direction. The variations in the mechanical strength between the printing direction corroborate the shear-induced partial alignment of CNTs, as shown previously with theoretical and experimental evidence (Figures 3 and S8C). The most significant increase in the mechanical strength between the mold-cast and the 3D-printed samples is observed for 0.1 wt %, and with increasing CNT loading, the percentage increase between the tensile strength of the mold-cast and the 3D-printed samples decreases (Figure S7). This is likely due to the difficulty in uniformly dispersing a high loading of CNTs in the viscous polymer matrix, regardless of the manufacturing technique. Nevertheless, thanks to DIW, even at high CNT loading (1 wt %), the 3D-printed samples outperformed the mold-cast samples in terms of their mechanical strength.

The Young's modulus values of the mold-cast and 3D-printed samples are presented in Figure 5B and show significantly higher values for 3D-printed samples (with a print path along the longitudinal direction) compared with their respective mold-cast counterparts. For example, the modulus improved from 2.94 \pm 0.22 to 4.26 \pm 0.03 GPa for 0.1 wt %, from 3.36 \pm 0.16 to 4.26 \pm 0.04 GPa for 0.3 wt %, and from 3.32 \pm 0.32 to 4.07 \pm 0.19 GPa for 1 wt % CNT loading. Interestingly, the 3D-printed samples with a print path along the transverse direction show improvement over mold-cast samples only for 0.1 wt %. For 0.3 and 1 wt %, the nanocomposites demonstrate equivalent values of Young's modulus as that of mold-cast samples. For this set of 3D-printed samples, since the applied load during the tensile test acts perpendicular to the direction of partial CNT alignment, these structures are prone to mechanical failure by delamination under certain stresses or orientations.

To shed further light on the observed differences in the mechanical properties, the fracture surface morphologies of the mold-cast and 3D-printed samples were

Article



analyzed under an SEM (Figures 5C-5H). Clearly, the fracture process and the fracture surface of the mold-cast (Figures 5C-5E) and the 3D-printed (Figures 5F-5H) samples are different. Although both samples display some degree of roughness (Figures 5C and 5F), which is typical of CNT-polymer nanocomposites, a closer look at higher resolution revealed that the surface of the mold-cast samples is smoother (Figures 5D and 5G). The relatively smooth surface of the mold-cast sample indicates generally uninterrupted crack propagation after a crack has been initiated. 30,55 Note that the presence of significant voids in the mold-cast samples (Figures 2A and S8A) can act as stress concentration zones and can easily initiate cracks. Furthermore, as can be seen in Figure 5C, the river-like pattern of radiating lines (marked by arrows) is a characteristic of rapid crack growth. On the other hand, for 3D-printed samples, the fracture surface appeared to have a greater degree of roughness (Figures 5F-5H). This suggests crack deflection and longer crack propagation length along different fracture planes. This might be due to the presence of uniformly distributed and welladhered CNTs, which can facilitate better stress transfer between the matrix and reinforcement. 30,55 The growth of a propagating crack front can be inhibited upon encountering a rigid obstacle—in this case, the well-dispersed CNTs. The crack front then has to move around the fillers to progress, which leads to the creation of two surfaces that join later at same or different heights. However, the crack may also propagate along the filler-matrix interface, leading to the creation of more fracture surfaces due to off-plane loading. This leads to the increase in surface roughness of the fracture surface, and as a result, more ridged patterns were observed throughout the fracture surface of 3D-printed samples (Figure 5H). Thus, creation of more surfaces and/or the joining of crack faces at different heights can be thought of as an indication of improved filler-matrix interfacial interaction⁵⁶ and thus should result in improved mechanical properties. Moreover, the mold-cast samples frequently displayed pockets of very smooth surface morphology (area marked by dotted line), where the reinforcing effects of CNTs are not observed (Figures 5E and S8B). Such smooth surface morphology is typically observed in neat epoxy samples. The frequent presence of such pockets suggests poor dispersion and regions susceptible to crack initiation and propagation. The co-existence of fracture-prone planes throughout the sample facilitates a continual crack path that requires less energy for the propagation of the crack.³⁰ Because of the observed microstructural changes, the 3D-printed samples demonstrated better performance than the mold-cast samples in terms of tensile strength and Young's modulus. Overall, due to the improved processing dynamics in 3D printing, there is a considerable improvement in microstructures and interfaces, which are critical for the fabrication of CNT-polymer nanocomposites with better mechanical and thermal properties.

In summary, architected CNT-epoxy nanocomposites with better mechanical and thermal properties were 3D printed from an engineered viscoelastic ink. This work demonstrates the potential of DIW in mitigating the conventional processing challenges of CNT-polymer composite fabrication, such as poor interfacial adhesion, wettability, and agglomeration. Thanks to the high shear force generated during the extrusion printing, the anisotropic CNT nanofillers undergo partial alignment within the 3D-printed samples along the print direction. We systematically show that the DIW technique provides a better microstructure and morphology compared with traditional mold-casting approaches. Consequently, the 3D-printed samples demonstrate superior thermal diffusivity, conductivity, and heat transfer mechanisms while having higher tensile strength and Young's modulus. This work demonstrates that DIW is not only useful in fabricating complex on-demand structures but that it also offers comprehensive advantages for composite fabrication by intrinsically improving the microstructure and physical properties. Such capabilities of





the 3D-printing process add to the engineering design and process optimization for realizing high-performance CNT-polymer nanocomposites.

EXPERIMENTAL PROCEDURES

Resource availability

Lead contact

Further information and requests for resources should be directed to and will be fulfilled by the lead contact, Muhammad M. Rahman (maksud@rice.edu).

Materials availability

All commercial chemicals were purchased from standard companies (Sigma-Aldrich and Millipore Sigma) and used without further purification. The study did not generate new, unique reagents.

Data and code availability

All data supporting and codes for analyzing the findings of this study are available within the article and are described in the supplemental information or are available from the lead contact upon reasonable request.

Formulation of CNT-epoxy nanocomposite ink

CNT-epoxy nanocomposite inks for DIW and mold casting were prepared by dispersing CNTs (multi-walled CNTs, Nanocyl NC7000) into a 3:1 formula of epoxy resin (Epon 826, Sigma Aldrich, and Jeffamine D230, Sigma Aldrich) using a planetary centrifugal mixer (THINKY MIXER ARE 310) at 2,000 rpm for 4 min. First, Epon 826 was heated to 100°C to reduce the viscosity for 10 min. CNTs at varying concentrations (0.1, 0.3, and 1 wt %) were added into the heated Epon 826 resin and mixed using the THINKY mixer. To reduce the viscosity for the facilitation of sonication, the CNT-epoxy formula was heated to 130°C for 10 min and transferred to a hot plate preheated to 100°C. The CNT-epoxy resin was sonicated for 30 min at 100°C at 50% amplitude using a probe sonicator (Q125 Sonicator). Following sonication, 8.5 wt % fumed silica (Sigma Aldrich, S5130–100G) was added and mixed using the THINKY mixer in three increments of 4 min at 2,000 rpm.

Mold casting

To cast the CNT-epoxy nanocomposite ink that was prepared following the fabrication section above, a stainless-steel dog bone mold (following ASTM d638) was greased to prevent adhesion of the nanocomposite to the mold. The CNT-epoxy nanocomposite ink was cast onto the greased mold. To prevent void expansion during curing, the ink was set for 48 h at room temperature, followed by a second curing step at 130°C for 1 h. The cured specimens were removed from the mold while still hot to prevent fracture and the introduction of residual stresses. After curing, the samples were polished to remove surface disparities.

3D printing of CNT-epoxy nanocomposites

CNT-epoxy nanocomposite ink was loaded into a 30 mL, Luer-Lock syringe and centrifuged to remove air bubbles. Smooth-flow tapered tips (Nordson EFD) were used to ensure further that any remaining air bubbles did not clog the tip during printing, which would cause non-uniform printing. Using a high-resolution 3D printer (Hyrel Engine HR), CNT-epoxy inks were extruded at room temperature onto silicone mats fixed to the 3D-printing build plate. Slic3r software was used to generate the G-code script for 3D printing based on the designed geometry and other programmed parameters, including extrusion width, printing speed, and layer height, to determine the printing path. The 3D-printed samples were cured following the

Article



same protocol as the mold-cast specimen. After 48 h at room temperature, the 3D-printed structures were heated to 130°C for 1 h. To 3D print dog bones, dimensions of the mold (ASTM d638) were recorded and replicated using a 20G tapered nozzle.

Rheological characterization

Rheological properties of inks were measured using ARES G2 Rheometer using a 25 mm flat plate geometry with a gap of 1,000 μ m. Flow and viscosity curves were obtained in strain-rate controlled measurement at shear rates from 1 to 1,000 s⁻¹. Oscillatory amplitude sweeps were performed at an angular frequency of 1 Hz with the strain from 0.01% to 10%.

Micrograph analysis

Optical images captured using a Zeiss Axio Scope.A1 at 20 × magnification and nodes of 3D-printed CNT-epoxy nanocomposites were captured using a Zeiss Stemi 200–CS at 0.65 magnification. Morphology and fracture surfaces were observed using a field-emission SEM (FEI Quanta 400) with 20 kV accelerating voltage. The surfaces were coated with a thin layer of gold (~10 nm) using a sputter coater to prevent charging. TEM micrographs were obtained using a JEOL 2110F TEM operated at 60 kV. TEM samples were prepared by polishing a thin specimen of CNT-epoxy to sub-1 mm using a hand-polishing method. The thin samples were cracked (pulled manually), and the edges of the fracture were investigated to observe CNT pullout. The optical image reported in Figure 1D was captured using an iPhone XR camera and color corrected to reduce warmth.

Raman spectroscopy

Raman spectroscopic mapping has been carried out using a Renishaw Raman spectrometer inVia confocal microscope. A green-colored laser line ($\lambda=532\,\text{nm}$) with a 5% laser energy source (solid-state, model RL53250) of 5 s exposure at 50× magnification was used for the investigation. The grating used was 1,800 groove/mm. The calibration of the instrument was carried out using an Si wafer at room temperature. The Raman modes of G and 2D peak were fitted through Lorentzian curve to interpret the peak shift. The spectrum of CNT powder has been used as a reference material.

Raman image analysis

The percentage of upshifting was calculated based on the ratio of number of pixels with hue values less than 150 (out of 256) to the total number of pixels. The two figures (Figure S4) show the selected regions that have hue values higher than 150. In our analysis, a hue value higher than 150 suggests no upshifting in the Raman modes and thus corresponds to Raman modes as observed in CNT powders or bundles.

UV-vis spectroscopy

UV-vis has been carried out using NanoDrop 2000 UV-Vis spectrophotometer. The range of wavelength of light used was 200–900 nm. Two samples were fabricated for the UV-vis experiment: (1) a "control" sample, which depicts the mold-cast sample where the ink does not undergo the 3D-printing extrusion process, and (2) an "extruded" sample, a representative of the 3D-printing case where the ink was extruded from a 3D-printing syringe. Therefore, the ink formulation and preparation of both samples are the same; however, we varied only the fact that the 3D-printed ink was extruded from a nozzle in order to subject the "extruded" ink to the forces responsible for increasing dispersion and the properties described in our work. The two formulations were then weighed, and an equal amount of acetone was added, followed by Thinky mixing and sonication, to make them dilute and dispersed enough for conducting solution-based UV-vis spectroscopy. In order to





quantitatively estimate the degree of CNT dispersion, the concentration of the exfoliated CNTs was calculated based on the Beer-Lambert law:

```
concentration of exfoliated CNTs = \frac{\text{specific absorbance at 500 nm}}{\text{specific extinction coefficient (at 500 nm)} * \text{length of light path}}
(Equation 2)
```

Here, the path length is 1 cm, and the extinction coefficient value for CNTs at 500 nm are considered in the range of $41.14-46 \text{ mL/mg-cm.}^{49}$

The percentage increase in the dispersion state, then, can be estimated using the following relation:

```
percentage increase in dispersion state = \frac{concentration of exfoliated CNTs}{initial CNT concentration}.
(Equation 3)
```

X-ray CT scans

X-ray CT scans were conducted at Aramco Americas (Houston, TX, USA) to show the variation of void formation in CNT-epoxy nanocomposites. X-ray CT scans were collected using an NSI X5000 Industrial CT scanner (North Star Imaging). The circular scans were performed at 720 views per rotation and a circular pitch of 50 μ m. The reconstructed radiographs were processed using ImageJ Volume Viewer.

Sample preparation for observing CNT alignment

Filaments of high CNT loading (2.75 wt %) were extruded from a 20G nozzle. To observe the CNT alignment along the extrusion direction, the filament was dissected into a cross-section parallel to the print path and was sputter coated to be observed under SEM.

Specific heat capacity

The specific heat at each temperature was calculated from the CNT-epoxy nano-composite specimen using a TA Instruments Q20 differential scanning calorimeter (DSC). The sample was heated at a ramp rate of 10 C min⁻¹ with nitrogen flow, and the specific heat was calculated following ASTM E1269-11.

Density measurements

A pycnometer (AcuPyc II) was used to measure the density of laser flash specimens. Ten density measurements were taken and averaged by the instrument.

Thermal conductivity

To measure thermal conductivity, CNT-epoxy nanocomposite samples containing 0.3 wt % CNTs were 3D printed. Sections of all samples were cut and polished into 1.2-mm-thick disks with a radius $\sim\!10$ mm. Thermal diffusivity was measured using the laser flash technique (LFA 457, Netzsch), and the thermal conductivity was calculated using $\kappa=dDC_p$, where d is the measured density, C_p is the specific heat capacity, and D is the measured diffusivity.

Heat transfer behavior

A white light from a supercontinuum laser (Fianium, WL–SC–400–8, 400–900 nm, 4 ps, 80 MHz) was applied for light-induced heating without further focusing (Beam Gaussian diameter D4 σ = 2.16 mm), while *in situ* surface temperatures were recorded with a thermal IR camera (FLIR, A615). A neutral density filter (Thorlabs, NDC–100C–4M) was applied to adjust the total power of illumination to 45 mW. Direct illumination of the thermal camera with our light source did not cause any observable increase in temperature, indicating that the illumination source has no

Article



mid-IR (2–10 μ m) photons. Therefore, the measured temperature rising during the experiments results only from photothermal heating effects rather than from scattering of the incident light. The incident light was aligned perpendicularly and centered on the top surface of the sample, and the thermal camera image was taken at 25° away from the incident light. The thermal images of the illuminated samples were then collected, and the temperature line profile along different directions on the sample surface was extracted for comparison.

Mechanical testing

All uniaxial in-plane tensile tests were conducted at room temperature using an MTS 858 servohydraulic machine in accordance with ASTM d638 type V scaled to a length of $\sim\!\!60$ cm and a width of $\sim\!\!9.5$ cm. The loading rate was 1 mm min $^{-1}$, and the span length was fixed for each sample at 30 mm. The test was performed using a 5 kN load cell, and the data were recorded until the specimen fractured. At least three specimens were tested for each formulation category to ensure the consistency of the data. The grips of 3D-printed dog bones were polished flat to fasten 3D-printed dog bones during testing.

SUPPLEMENTAL INFORMATION

Supplemental information can be found online at https://doi.org/10.1016/j.xcrp. 2023.101617.

ACKNOWLEDGMENTS

The authors gratefully acknowledge financial support from Aramco Research Center (grant reference number: 1137681) and Carbon Hub, Rice University. The authors also acknowledge the support of Qiushi Sun and the Reservoir Engineering Technology Team at Aramco Americas, Houston, for providing the CT images and Georgesha Ross and the Drilling Technology team at Aramco Americas, Houston, for providing SEM images related to CNT alignment in 3D-printed epoxy specimens. M.T. and A.B.D. are thankful for strategic development funding from the University of Sussex. H.Z. acknowledges the financial support from National Science Foundation (NSF DMR 2005096).

AUTHOR CONTRIBUTIONS

A.Z.K. designed the experiments, implemented the experiments, analyzed the data, and wrote the manuscript. M.A.S.R.S. provided experimental suggestions, implemented the experiments, analyzed the data, and wrote the manuscript. S.B. analyzed the data and edited the manuscript. A.K. conducted theoretical calculations. M.T. and M.K. implemented the experiments and analyzed the data. S.S., M.L., M.B., M.M., and V.H. implemented the experiments. A.B.D., N.K., C.S.T., P.J.B., B.Y., and H.Z. provided expertise and experimental suggestions. P.M.A. provided financial support and supervised the research. M.M.R. conceived the original idea, provided financial support, supervised the research, and reviewed and edited the manuscript.

DECLARATION OF INTERESTS

The authors declare no competing interests.

Received: September 17, 2022

Revised: July 2, 2023

Accepted: September 8, 2023 Published: October 2, 2023



Cell Reports Physical Science Article

REFERENCES

- Schadler, L.S., Giannaris, S.C., and Ajayan, P.M. (1998). Load transfer in carbon nanotube epoxy composites. Appl. Phys. Lett. 73, 3842–3844. https://doi.org/10.1063/1.122911.
- Rahman, M.M., Zainuddin, S., Hosur, M.V., Malone, J.E., Salam, M.B.A., Kumar, A., and Jeelani, S. (2012). Improvements in mechanical and thermo-mechanical properties of e-glass/ epoxy composites using amino functionalized MWCNTs. Compos. Struct. 94, 2397–2406. https://doi.org/10.1016/j.compstruct.2012. 03.014.
- Byrne, M.T., and Gun'ko, Y.K. (2010). Recent Advances in Research on Carbon Nanotube-Polymer Composites. Adv. Mater. 22, 1672– 1688. https://doi.org/10.1002/adma. 200901545
- 4. Ajayan, P.M., Schadler, L.S., Giannaris, C., and Rubio, A. (2000). Single-Walled Carbon Nanotube-Polymer Composites: Strength and Weakness. Adv. Mater. 12, 750–753. https:// doi.org/10.1002/(SICI)1521-4095(200005) 12:10<750::AID-ADMA750>3.0.CO;2-6.
- Chen, J., Yan, L., Song, W., and Xu, D. (2018). Interfacial characteristics of carbon nanotube-polymer composites: A review. Compos. Appl. Sci. Manuf. 114, 149–169. https://doi.org/10. 1016/i.compositesa.2018.08.021.
- Rahman, M.M., Zainuddin, S., Hosur, M.V., Robertson, C.J., Kumar, A., Trovillion, J., and Jeelani, S. (2013). Effect of NH2-MWCNTs on crosslink density of epoxy matrix and ILSS properties of e-glass/epoxy composites. Compos. Struct. 95, 213–221. https://doi.org/ 10.1016/j.compstruct.2012.07.019.
- Rahman, M., Hosur, M., Zainuddin, S., Vaidya, U., Tauhid, A., Kumar, A., Trovillion, J., and Jeelani, S. (2013). Effects of aminofunctionalized MWCNTs on ballistic impact performance of E-glass/epoxy composites using a spherical projectile. Int. J. Impact Eng 57, 108–118. https://doi.org/10.1016/j. ijimpeng.2013.01.011.
- Coleman, J.N., Khan, U., Blau, W.J., and Gun'ko, Y.K. (2006). Small but strong: A review of the mechanical properties of carbon nanotube–polymer composites. Carbon 44, 1624–1652. https://doi.org/10.1016/j.carbon. 2006.02.038.
- Pramanik, C., Gissinger, J.R., Kumar, S., and Heinz, H. (2017). Carbon Nanotube Dispersion in Solvents and Polymer Solutions: Mechanisms, Assembly, and Preferences. ACS Nano 11, 12805–12816. https://doi.org/10. 1021/acsnano.7b07684.
- Fernandes, R.M.F., Abreu, B., Claro, B., Buzaglo, M., Regev, O., Furó, I., and Marques, E.F. (2015). Dispersing Carbon Nanotubes with Ionic Surfactants under Controlled Conditions: Comparisons and Insight. Langmuir 31, 10955– 10965. https://doi.org/10.1021/acs.langmuir. 5502050
- Zainuddin, S., Fahim, A., Arifin, T., Hosur, M.V., Rahman, M.M., Tyson, J.D., and Jeelani, S. (2014). Optimization of mechanical and thermo-mechanical properties of epoxy and E-glass/epoxy composites using NH2-MWCNTs, acetone solvent and combined dispersion methods. Compos. Struct. 110,

- 39–50. https://doi.org/10.1016/j.compstruct. 2013.11.010.
- Mallakpour, S., and Soltanian, S. (2016). Surface functionalization of carbon nanotubes: fabrication and applications. RSC Adv. 6, 109916–109935. https://doi.org/10.1039/ C6RA24522F.
- Banerjee, S., Hemraj-Benny, T., and Wong, S.S. (2005). Covalent Surface Chemistry of Single-Walled Carbon Nanotubes. Adv. Mater. 17, 17–29. https://doi.org/10.1002/adma. 200401340.
- Sahoo, N.G., Rana, S., Cho, J.W., Li, L., and Chan, S.H. (2010). Polymer nanocomposites based on functionalized carbon nanotubes. Prog. Polym. Sci. 35, 837–867. https://doi.org/ 10.1016/j.progpolymsci.2010.03.002.
- Ngo, T.D., Kashani, A., Imbalzano, G., Nguyen, K.T., and Hui, D. (2018). Additive manufacturing (3D printing): A review of materials, methods, applications and challenges. Compos. B Eng. 143, 172–196. https://doi.org/10.1016/j. compositesb.2018.02.012.
- du Plessis, A., Broeckhoven, C., Yadroitsava, I., Yadroitsev, I., Hands, C.H., Kunju, R., and Bhate, D. (2019). Beautiful and Functional: A Review of Biomimetic Design in Additive Manufacturing. Addit. Manuf. 27, 408–427. https://doi.org/10.1016/j.addma.2019.03.033.
- Maguire, A., Pottackal, N., Saadi, M.A.S.R., Rahman, M.M., and Ajayan, P.M. (2020). Additive manufacturing of polymer-based structures by extrusion technologies. Oxf. Open Mater. Sci. 1. https://doi.org/10.1093/ oxfmat/itaa004.
- Lewis, J. (2006). Direct Ink Writing of 3D Functional Materials. Adv. Funct. Mater. 16, 2193–2204. https://doi.org/10.1002/adfm. 200600434.
- Tagliaferri, S., Panagiotopoulos, A., and Mattevi, C. (2021). Direct ink writing of energy materials. Mater. Adv. 2, 540–563. https://doi. org/10.1039/D0MA00753F.
- Sajadi, S.M., Tiwary, C.S., Rahmati, A.H., Eichmann, S.L., Thaemlitz, C.J., Salpekar, D., Puthirath, A.B., Boul, P.J., Rahman, M.M., Meiyazhagan, A., and Ajayan, P.M. (2021). Deformation resilient cement structures using 3D-printed molds. iScience 24, 102174. https:// doi.org/10.1016/j.isci.2021.102174.
- Saadi, M.A.S.R., Maguire, A., Pottackal, N.T., Thakur, M.S.H., Ikram, M.M., Hart, A.J., Ajayan, P.M., and Rahman, M.M. (2022). Direct Ink Writing: A 3D Printing Technology for Diverse Materials. Adv. Mater. 34, 2108855. https://doi. org/10.1002/adma.202108855.
- 22. Yuk, H., and Zhao, X. (2018). A New 3D Printing Strategy by Harnessing Deformation, Instability, and Fracture of Viscoelastic Inks. Adv. Mater. 30, 1704028. https://doi.org/10.1002/adma.201704028.
- Compton, B.G., and Lewis, J.A. (2014). 3D Printing: 3D-Printing of Lightweight Cellular Composites (Adv. Mater. 34/2014). Adv. Mater. 26, 6043. https://doi.org/10.1002/adma. 201470235.

- Hausmann, M.K., Rühs, P.A., Siqueira, G., Läuger, J., Libanori, R., Zimmermann, T., and Studart, A.R. (2018). Dynamics of Cellulose Nanocrystal Alignment during 3D Printing. ACS Nano 12, 6926–6937. https://doi.org/10. 1021/acsnano.8b02366.
- Lewicki, J.P., Rodriguez, J.N., Zhu, C., Worsley, M.A., Wu, A.S., Kanarska, Y., Horn, J.D., Duoss, E.B., Ortega, J.M., Elmer, W., et al. (2017). 3D-Printing of Meso-structurally Ordered Carbon Fiber/Polymer Composites with Unprecedented Orthotropic Physical Properties. Sci. Rep. 7, 43401. https://doi.org/ 10.1038/srep43401.
- Jambhulkar, S., Liu, S., Vala, P., Xu, W., Ravichandran, D., Zhu, Y., Bi, K., Nian, Q., Chen, X., and Song, K. (2021). Aligned Ti ₃ C ₂ T _x MXene for 3D Micropatterning via Additive Manufacturing. ACS Nano 15, 12057–12068. https://doi.org/10.1021/acsnano.1c03388.
- Jiang, Q., Zhang, H., Rusakov, D., Yousefi, N., and Bismarck, A. (2021). Additive Manufactured Carbon Nanotube/Epoxy Nanocomposites for Heavy-Duty Applications. ACS Appl. Polym. Mater. 3, 93–97. https://doi. org/10.1021/acsapm.0c01011.
- Sarmah, A., Desai, S.K., Crowley, A.G., Zolton, G.C., Tezel, G.B., Harkin, E.M., Tran, T.Q., Arole, K., and Green, M.J. (2022). Additive manufacturing of nanotube-loaded thermosets via direct ink writing and radio-frequency heating and curing. Carbon 200, 307–316. https://doi.org/10.1016/j.carbon.2022.08.063.
- Jajam, K.C., Rahman, M.M., Hosur, M.V., and Tippur, H.V. (2014). Fracture behavior of epoxy nanocomposites modified with polyol diluent and amino-functionalized multi-walled carbon nanotubes: A loading rate study. Compos. Appl. Sci. Manuf. 59, 57–69. https://doi.org/10. 1016/j.compositesa.2013.12.014.
- Rahman, M.M., Hosur, M., Zainuddin, S., Jajam, K.C., Tippur, H.V., and Jeelani, S. (2012). Mechanical characterization of epoxy composites modified with reactive polyol diluent and randomly-oriented aminofunctionalized MWCNTs. Polym. Test. 31, 1083–1093. https://doi.org/10.1016/j. polymertesting.2012.08.010.
- Neumann, T.V., and Dickey, M.D. (2020). Liquid Metal Direct Write and 3D Printing: A Review. Adv. Mater. Technol. 5, 2000070. https://doi. org/10.1002/admt.202000070.
- Hmeidat, N.S., Kemp, J.W., and Compton, B.G. (2018). High-strength epoxy nanocomposites for 3D printing. Compos. Sci. Technol. 160, 9–20. https://doi.org/10.1016/j.compscitech. 2018.03.008.
- Payne, A.R. (1962). The dynamic properties of carbon black-loaded natural rubber vulcanizates. Part I. J. Appl. Polym. Sci. 6, 57–63. https://doi.org/10.1002/app.1962. 070061906.
- Medalia, A.I. (1978). Effect of Carbon Black on Dynamic Properties of Rubber Vulcanizates. Rubber Chem. Technol. 51, 437–523. https://doi.org/10.5254/1.3535748.
- 35. Fletcher, W.P., and Gent, A.N. (1954). Nonlinearity in the Dynamic Properties of

Article



- Vulcanized Rubber Compounds. Rubber Chem. Technol. 27, 209–222. https://doi.org/10.5254/1.3543472
- Wang, M.-J. (1999). The Role of Filler Networking in Dynamic Properties of Filled Rubber. Rubber Chem. Technol. 72, 430–448. https://doi.org/10.5254/1.3538812.
- Preghenella, M., Pegoretti, A., and Migliaresi, C. (2005). Thermo-mechanical characterization of fumed silica-epoxy nanocomposites. Polymer 46, 12065–12072. https://doi.org/10. 1016/j.polymer.2005.10.098.
- Barthel, H., Dreyer, M., Gottschalk-Gaudig, T., Litvinov, V., and Nikitina, E. (2002). Fumed silica – rheological additive for adhesives, resins, and paints. Macromol. Symp. 187, 573–584. https://doi.org/10.1002/1521-3900(200209)187:1<573::AID-MASY573>3.0. CO;2-1.
- Paquien, J.-N., Galy, J., Gérard, J.-F., and Pouchelon, A. (2005). Rheological studies of fumed silica-polydimethylsiloxane suspensions. Colloids Surf. A Physicochem. Eng. Asp. 260, 165–172. https://doi.org/10. 1016/j.colsurfa.2005.03.003.
- Kim, Y., Yuk, H., Zhao, R., Chester, S.A., and Zhao, X. (2018). Printing ferromagnetic domains for untethered fast-transforming soft materials. Nature 558, 274–279. https://doi. org/10.1038/s41586-018-0185-0.
- Peigney, A., Flahaut, E., Laurent, C., Chastel, F., and Rousset, A. (2002). Aligned carbon nanotubes in ceramic-matrix nanocomposites prepared by high-temperature extrusion. Chem. Phys. Lett. 352, 20–25. https://doi.org/ 10.1016/S0009-2614(01)01441-5.
- Li, Y., and Seidel, G.D. (2018). Multiscale modeling of the interface effects in CNT-epoxy nanocomposites. Comput. Mater. Sci. 153,

- 363–381. https://doi.org/10.1016/j.commatsci. 2018.07.015.
- Anvari, A. (2020). The Influence of CNT Structural Parameters on the Properties of CNT and CNT-Reinforced Epoxy. International Journal of Aerospace Engineering 2020, e4873426. https://doi.org/10.1155/2020/ 4873426.
- Vašková, H., and Kresalek, V. (2011). Raman spectroscopy of epoxy resin crosslinking. In Recent Researches in Automatic Control, p. 6.
- Xu, Z., He, Z., Song, Y., Fu, X., Rommel, M., Luo, X., Hartmaier, A., Zhang, J., and Fang, F. (2018). Topic Review: Application of Raman Spectroscopy Characterization in Micro/Nano-Machining. Micromachines 9, 361. https://doi. org/10.3390/mi9070361.
- Jorio, A., and Saito, R. (2021). Raman spectroscopy for carbon nanotube applications. J. Appl. Phys. 129, 021102. https://doi.org/10.1063/5.0030809.
- Yoshikawa, M., Murakami, M., and Fujita, Y. (2022). Structural characterization of intersections between semiconducting and metallic carbon nanotubes using tip-enhanced Raman spectroscopy. J. Raman Spectrosc. 53, 1048–1054. https://doi.org/10.1002/jrs.6344.
- Bokobza, L. (2012). Raman spectroscopic characterization of multiwall carbon nanotubes and of composites. Express Polym. Lett. 6, 601–608. https://doi.org/10.3144/ expresspolymlett.2012.63.
- Korayem, A.H., Barati, M.R., Chen, S.J., Simon, G.P., Zhao, X.L., and Duan, W.H. (2015). Optimizing the degree of carbon nanotube dispersion in a solvent for producing reinforced epoxy matrices. Powder Technol. 284, 541–550. https://doi.org/10.1016/j.powtec.2015.07.023.

- Yu, J., Grossiord, N., Koning, C.E., and Loos, J. (2007). Controlling the dispersion of multi-wall carbon nanotubes in aqueous surfactant solution. Carbon 45, 618–623. https://doi.org/ 10.1016/j.carbon.2006.10.010.
- Liu, J., Guo, Y., Weng, C., Zhang, H., and Zhang, Z. (2020). High thermal conductive epoxy based composites fabricated by multimaterial direct ink writing. Compos. Appl. Sci. Manuf. 129, 105684. https://doi.org/10.1016/j. compositesa.2019.105684.
- Jeffery, G.B. (1922). The motion of ellipsoidal particles immersed in a viscous fluid. Proc. Roy. Soc. Lond. A 102, 161–179. https://doi.org/10. 1098/rspa.1922.0078.
- Marconnet, A.M., Yamamoto, N., Panzer, M.A., Wardle, B.L., and Goodson, K.E. (2011). Thermal Conduction in Aligned Carbon Nanotube–Polymer Nanocomposites with High Packing Density. ACS Nano 5, 4818–4825. https://doi.org/10.1021/nn200847u.
- Parker, W.J., Jenkins, R.J., Butler, C.P., and Abbott, G.L. (1961). Flash Method of Determining Thermal Diffusivity, Heat Capacity, and Thermal Conductivity. J. Appl. Phys. 32, 1679–1684. https://doi.org/10.1063/1. 1728417.
- Ma, P.-C., Mo, S.-Y., Tang, B.-Z., and Kim, J.-K. (2010). Dispersion, interfacial interaction and re-agglomeration of functionalized carbon nanotubes in epoxy composites. Carbon 48, 1824–1834. https://doi.org/10.1016/j.carbon. 2010.01.028.
- Chakraborty, S., Chakraborty, A.K., Barbezat, M., and Terrasi, G.P. (2018). Interfacial interaction and the fracture toughness (K IC) trends in epoxy nanocomposites filled with functionalized graphene-based fillers. Polym. Compos. 39, E2356–E2369. https://doi.org/10. 1002/pc.24675.